JOURNAL OF AIRCRAFT
Vol. 41, No. 2, March–April 2004

Models for Aeroservoelastic Analysis with Smart Structures

Moti Karpel* and Boris Moulin†
Technion, Israel Institute of Technology, 32000 Haifa, Israel

Modal-based mathematical models for the analysis of control-augmented aeroelastic systems are expanded to facilitate the use of distributed strain actuators. Smart actuators are constructed of structural elements, such as piezoelectric patches, that change their shape due to electric inputs. When embedded in the structure, the deforming smart elements introduce structural strains that change the shape of the structure and, consequently, the aerodynamic load distribution. The voltage–strain relations, the overdetermined nature of the elastic actuator–structure equilibrium, the relatively large number of involved interface coordinates, and the high importance of local strains that typically limit the actuator performance require substantial modifications in the modeling process compared to that with common control-surface actuators. Fictitious masses are used in a way that causes the inclusion of important actuator strain information in the modal data with a minimal increase in the number of structural states. A control mode is defined by the static deformations due to a unit static voltage command. Huge dummy masses may be used to generate the control modes as part of a standard normal-modes analysis. State-space aeroservoelastic equations are constructed by the use of the minimum-state rational aerodynamic approximation approach. Two options are given for the introduction of control forces: a direct application of the forces, and an indirect application through the control mode. A numerical application for an unmanned aerial vehicle with a piezoelectric-driven control surface demonstrates the two options and shows that the control-mode option has some numerical advantages.

Introduction

THE use of smart-structure technology to control the structural dynamic stability and response of air vehicles attracted extensive research and development efforts in recent years.[1−3] Smart structural components such as piezoelectric patches are embedded in the structure and subjected to electric inputs that cause the structure to change its shape. The shape changes introduce internal forces that deform the surrounding structure and participate in its aeroelastic behavior. The application of standard modeling methods for deriving modal-based state-space equations for aeroservoelastic (ASE) analysis with smart structures is desired. A major problem is that the standard modal approach might not consider the deformations at and near the smart components adequately. These deformations are vital for a proper evaluation of the smart-structure performance and integrity.

The fictitious-mass (FM) method[4,5] can be used to enforce selected local deformations in the set of low-frequency modes taken into account in the modal-based analysis. The normal modes are calculated with selected degrees of freedom loaded by large FMs. Their dynamic effects are later removed, leaving the modal basis with a set of local deformation modes to be included in the subsequent modal-based analyses. FM were used for modal coupling in aircraft-store flutter analysis,[4,6] for eigenvalue analysis of control augmented structures,[7] time domain flutter analysis with large structural variations,[8,9] and dynamic response to impulsive excitation.[10] FM concepts were also used in modal tests of structural components loaded with added boundary masses.[11,12] The added masses caused the measured data to contain more near-boundary information, which improved subsequent modal coupling and model update processes.

The effectiveness of the FM method is reduced with increasing numbers of FMs in the model because it requires a larger number of modes to be taken into account. This might be a problem in smart-structure applications because the adequate number of interface coordinates between the smart patches and the structure can be relatively large. On the other hand, the balance of internal forces in smart patches facilitate the application of special FM matrices that reduce the number of added modes. One of the purposes of this research is to modify the FM method such that it can yield adequate local stresses in subsequent analyses with a minimal number of added modes. The new formulation reduces the effects of the FMs on the regular elastic normal modes and eliminates the effects on rigid-body mass properties.

In addition to causing inefficiency in subsequent analyses, an expanded modal database might cause numerical difficulties in the aerodynamic rational approximation process that is needed for ASE analysis. These numerical difficulties are investigated in the paper and a solution is obtained by the definition control modes with the shape of the static structural deformations due to unit electric input.

It should be emphasized that the applicability of piezoelectric materials for shape control of aerospace structures is still quite limited due to their fragility, small deformations, and insufficient power efficiency.[1,2] However, considerable research and development efforts are being made to expand the material applicability.[1,2] A major purpose of the research presented in this paper is to support these efforts. Furthermore, as will be shown, the formulation of the actuators is based on the their deformations due to unit commands, their stiffness properties and the interface geometry with the controlled structure. Hence, even though the actuators in this paper are assumed to be constructed of piezoelectric materials, the formulation is directly applicable to any set of linear actuators with overdeterminate interface of the structure.

Normal Modes with FM

A major disadvantage of the modal approach is its inaccuracy in predicting a local response to concentrated loads. This difficulty can be cured by adding large FMs at the points of force application when the normal modes are calculated.[7] The eigenproblem of the actual structure is replaced by

$$[K_{aa}][\phi_{ai}] = [M_{aa} + M_F][\phi_{ai}][\Omega_i] \tag{1}$$

Presented as Paper 2002-1290 at the AIAA/ASME/ASCE/AHS/ASC 43rd Structural Dynamics Meeting, Denver, CO, 22 April 2002; received 15 July 2002; revision received 6 October 2003; accepted for publication 6 October 2003.

*Professor, Sanford Kaplan Chair in Aerospace Engineering, Faculty of Aerospace Engineering. Associate Fellow AIAA.

†Senior Researcher, Faculty of Aerospace Engineering. Member AIAA.

where $[K_{aa}]$ and $[M_{aa}]$ are the full discrete-coordinate stiffness and mass matrices and $[M_F]$ is a matrix of the added FMs at desired locations. Standard eigenproblem codes can be used for solving Eq. (1) for a relatively small set of low eigenvalues that form the diagonal $[\Omega_i]$ and the associated eigenvector matrix (mode shapes) $[\phi_{ai}]$. With relatively large FMs, $[\phi_{ai}]$ contains significant local deformation at the vicinity of the FMs, which implies high-fidelity representation of these locations in the modal basis. The eigenvalues and eigenvectors are, of course, substantially different than those of the actual structure. However, by assuming that the actual normal modes are linear combinations of $[\phi_{ai}]$, we can resort to the actual model by removing the effect of $[M_F]$ from the generalized mass matrix by

$$[\tilde{M}_{ii}] = [M_{ii}] - [\phi_{ai}]^T [M_F][\phi_{ai}] \tag{2}$$

where

$$[M_{ii}] = [\phi_{ai}]^T [M_{aa} + M_F][\phi_{ai}]$$

is the diagonal generalized mass matrix associated with the eigenproblem of Eq. (1). The nondiagonal $[\tilde{M}_{ii}]$ of Eq. (2) and the diagonal generalized stiffness matrix $[K_{ii}]$ associated with Eq. (1) form the eigenvalue problem

$$[K_{ii}][\psi] = [\tilde{M}_{ii}][\psi][\Omega_h] \tag{3}$$

that, being of low order, can be easily solved for all of its eigenvalues $[\Omega_h]$ and eigenvectors $[\psi]$, with $[\psi]$ normalized such that

$$[M_{hh}] = [\psi]^T [M_{ii}][\psi] = [I], \qquad [K_{hh}] = [\psi]^T [K_{ii}][\psi] = [\Omega_h] \tag{4}$$

The mode shapes after removing the FMs are recovered by

$$[\phi_{ah}] = [\phi_{ai}][\psi] \tag{5}$$

The low eigenvalues in $[\Omega_h]$, and the associated modes in $[\phi_{ah}]$, are typically almost identical to those of the nominal finite element model. The highest-frequency modes reflect local deformations and are not necessarily actual physical natural modes. They are sought out, however, to account for local deformations in subsequent analyses. The number of these local-deformation modes is up to the rank of $[M_F]$, depending on the number of modes taken into account and the size of the FM terms.

The application of piezoelectric patches or stacks as control actuators requires good evaluation of the strains and stresses in the piezoelectric material and the local structural area to which the actuators are connected. The use of FMs at the actuator–structure interface coordinates may provide a convenient way for an adequate evaluation of the local behavior. The main difficulty is that a large number of interface coordinates might yield a relatively large number of modal coordinates in the resulting ASE model. Besides the addition of a numerical burden, a large number of modal coordinates might cause severe numerical difficulties in the aerodynamic approximation part of the modeling process and in the control design process.

A way to reduce the number of additional modes due to the ith patch is by the use of an FM matrix $[M_{F_i}]$, which is proportional to the associated free–free patch stiffness matrices $[K_{p_i}]$. The rank of this singular matrix is only the number of overdetermined coordinates. In addition, as demonstrated in the numerical example, the effect of the FMs on the regular normal modes is typically small, which helps in the selection of modal coordinates.

Piezoelectric Actuator Forces

The piezoelectric actuators in this work are elastic patches that change their shape when subjected to electric voltage. When attached to the structure, the shape-change attempt causes structural deformations. A patch is characterized by the displacement vector of its interface grid points $\{x_{c_i}\}$ due to a unit voltage input when the patch is restrained in a statically determined manner, but not attached to the structure. It is assumed at this stage that the dependency of $\{x_{c_i}\}$ on the associated voltage input v_{p_i} is linear and independent of the excitation frequency. Other displacement-voltage dependencies can be modeled as part of the control system.

When attached to the structure, the discrete elastic forces applied by a piezoelectric patch to the structure are

$$\{F_{p_i}(t)\} = [K_{p_i}]\left(\{x_{c_i}\} v_{p_i}(t) - \{u_{p_i}(t)\}\right) \tag{6}$$

where $[K_{p_i}]$ is the free–free stiffness matrix of the ith patch and $\{u_{p_i}\}$ is the actual displacement vector at the patch–structure interface grid points.

With the stiffness matrices of the piezoelectric patches added to the stiffness matrix of the structure, the static equilibrium equation of the structure under loads generated by piezoelectric voltage is

$$[K_{aa}]\{u_a\} = [K^p_{aa}][X_{ap}]\{v_p(t)\} \tag{7}$$

where $[K^p_{aa}]$ is a zero matrix except for the contributions of the stiffness matrices $[K_{p_i}]$ of the patches, $[X_{ap}]$ is a zero matrix except for the patch unit-command displacements $\{x_{c_i}\}$ at the patch-related degrees of freedom in the respective columns, and $\{v_p\}$ is the vector of piezoelectric voltage inputs. The forces in the right-hand side of Eq. (7) are those obtained when the patched are connected to a rigid structure. Piezoelectric devices are often characterized by the maximal values of these forces.

The modal approach assumes that

$$\{u_a\} = [\phi_{ah}]\{\xi\} \tag{8}$$

where $\{\xi\}$ is the vector of generalized displacements. The resulting generalized-coordinate version of Eq. (7) is

$$[K_{hh}]\{\xi\} = [\phi_{ah}]^T [K^p_{aa}][X_{ap}]\{v_p(t)\} \tag{9}$$

The zero eigenvalues and the associated rigid-body modes $[\phi_{ah_r}]$ are truncated to avoid singularity. This truncation is valid because the piezoelectric generalized forces on the rigid-body modes are zero, as can be deduced from the fact that the free–free piezoelectric patch stiffness matrices must satisfy $[\phi_{ah_r}]^T [K^p_{aa}] = [0]$.

The solution of Eq. (9) with $\{v_p\} = \{I_i\}$, namely, a zero vector except for $v_{p_i} = 1$, and the substitution of the resulting $\{\xi\}$ in Eq. (8), yield the vector of structural displacements due to the ith unit piezoelectric command in the absence of aerodynamic forces. The assembly of the displacement vectors due to separate unit voltage commands,

$$[\phi_{ap}] = [\phi_{ah}][K_{hh}]^{-1}[\phi_{ah}]^T [K^p_{aa}][X_{ap}] \tag{10}$$

is referred to here the matrix of piezoelectric control modes. It can be obtained with adequate accuracy only if FMs are used, as discussed earlier, such that local deformations at the patch vicinity appear in the group of high-frequency normal modes taken into account. An alternative way for generating control modes is discussed hereafter.

The inclusion of piezoelectric actuators in the ASE equations of motion is presented hereafter in two ways, one in which the piezoelectric forces are applied directly, similarly to Eq. (9), and one through the definition of piezoelectric control modes.

Aeroelastic Equations with Direct Piezoelectric Control Forces

The open-loop aeroelastic equations of motion with conventional actuator-driven control surfaces are based on the rational approximation of the unsteady aerodynamic force coefficient matrices, in the Laplace domain, of the form[10,11]

$$[\tilde{Q}_h(s)] = [A_{h0}] + (b/V)[A_{h1}]s + (b^2/V^2)[A_{h2}]s^2 + [D_h][[I]s - (V/b)[R]]^{-1}[E]s \tag{11}$$

where the $[A_{hi}]$ and $[E]$ matrices are column partitioned according to the structural and control modes as

$$[A_{hn}] = \begin{bmatrix} A_{hh_n} & A_{hc_n} \end{bmatrix}, \qquad n = 0, 1, 2$$

$$[E] = [E_h \quad E_c]$$

The coefficient matrices in Eq. (11) are determined in a nonlinear least-square solution that approximates a set of force coefficients matrices $[Q_h(ik)]$ determined for harmonic oscillations at several tabulated reduced-frequency values $k = \omega b/V$, where ω is the frequency of oscillations, b is a reference semichord, and V is the air velocity.

The resulting state-space equation of motion of the open-loop aeroelastic system excited by control-surface deflection commands $\{\delta_c(t)\}$ and piezoelectric voltage inputs $\{v(t)\}$ as in Eq. (9) is

$$\{\dot{x}_{ae}\} = [A_{ae}]\{x_{ae}\} + [B_{ae}]\{u_{ae}\} + \begin{bmatrix} B^p_{ae} \end{bmatrix}\begin{Bmatrix} u^p_{ae} \end{Bmatrix} \tag{12}$$

where

$$\{x_{ae}\} = \begin{Bmatrix} \xi \\ \dot{\xi} \\ x_a \end{Bmatrix}, \qquad \{u_{ae}\} = \begin{Bmatrix} \delta_c \\ \dot{\delta}_c \\ \ddot{\delta}_c \end{Bmatrix}, \qquad \begin{Bmatrix} u^p_{ae} \end{Bmatrix} = \{v_p\}$$

where $\{\xi\}$ is the vector of n_h modal displacements taken into account, $\{x_a\}$ is the vector of n_a aerodynamic states where n_a is the size of $[R]$ in Eq. (10), and

$$[A_{ae}] = \begin{bmatrix} 0 & [I] & 0 \\ -[\bar{M}]^{-1}[\bar{K}] & -[\bar{M}]^{-1}[\bar{B}] & -q[\bar{M}]^{-1}[D_h] \\ 0 & [E_h] & \dfrac{V}{b}[R] \end{bmatrix}$$

$$[B_{ae}] = \begin{bmatrix} 0 & 0 & 0 \\ -[\bar{M}]^{-1}[\bar{K}_{hc}] & -[\bar{M}]^{-1}[\bar{B}_{hc}] & -[\bar{M}]^{-1}[\bar{M}_{hc}] \\ 0 & [E_c] & 0 \end{bmatrix}$$

$$\begin{bmatrix} B^p_{ae} \end{bmatrix} = \begin{bmatrix} 0 \\ [\bar{M}]^{-1}[\phi_{ah}]^T \begin{bmatrix} K^p_{aa} \end{bmatrix}[X_{ap}] \\ 0 \end{bmatrix}$$

and where

$$[\bar{M}] = [M_{hh}] + (qb^2/V^2)\begin{bmatrix} A_{hh_2} \end{bmatrix}, \qquad [\bar{K}] = \begin{bmatrix} K_{hh} + qA_{hh_0} \end{bmatrix}$$

$$[\bar{B}] = \begin{bmatrix} B_{hh} + (qb/V)A_{hh_1} \end{bmatrix}, \qquad [\bar{M}_{hc}] = \begin{bmatrix} M_{hc} + (qb^2/V^2)A_{hc_2} \end{bmatrix}$$

$$[\bar{K}_{hc}] = q\begin{bmatrix} A_{hc_0} \end{bmatrix}, \qquad [\bar{B}_{hc}] = (qb/V)\begin{bmatrix} A_{hc_1} \end{bmatrix}$$

Because the deformations due to piezoelectric commands and the associated aerodynamic forces are expressed mainly through the high-frequency modes generated by the FMs, as argued after Eq. (10), these modes must be included in the aerodynamic approximations and the state-space equations. This might yield numerical difficulties in the aerodynamic approximation process and in the resulting stability characteristics. The modeling option shown hereafter, which uses explicit piezoelectric control modes, may alleviate this problem.

The output parameters are expressed in the form

$$\{y_{ae}\} = [C_{ae}]\{x_{ae}\} + [D_{ae}]\{u_{ae}\} + \begin{bmatrix} D^p_{ae} \end{bmatrix}\begin{Bmatrix} u^p_{ae} \end{Bmatrix} \tag{13}$$

Structural displacements, velocities, and accelerations can be cast in the form of Eq. (13) by the mode-displacement approach.[10] Stresses and strains, which are often critical parameters in the performance evaluation of piezoelectric actuators, can also be adequately expressed in terms of modal displacements when FMs are used. Structural element strains, for example, are related to the generalized displacements $\{\xi\}$ (which are part of $\{x_{ae}\}$) by

$$\{\epsilon_s\} = [EU_{sa}][\phi_{ah}]\{\xi\} \tag{14}$$

where $[EU]$ is the matrix that relates strains to displacements. However, strains in the piezoelectric material require an additional term due to the voltage input

$$\{\epsilon_p\} = [EU_{pa}]([\phi_{ah}]\{\xi\} - [X_{ap}])\{v_p\} \tag{15}$$

The two types of input parameters in Eqs. (12) and (13) are separated because they are treated differently in the subsequent ASE equations. Whereas the piezoelectric $\{u^p_{ae}\}$ voltage commands are kept as direct input parameters, the control-surface input vector, $\{u_{ae}\} = [\delta \;\; \dot{\delta} \;\; \ddot{\delta}]^T$, becomes part of the state vector as a result of adding a third-order actuator model[11] for each control surface. The resulting input parameters are the actuator input commands δ_c. Higher-order actuators can be modeled as part of the control system.

The actuator inputs $\{\delta_c\}$ and piezoelectric commands $\{v_p\}$ can be combined for a single plant input vector in a standard state-space formulation. A control system can then be augmented and applied in ASE analyses as described in Ref. 13.

Generation of Control Modes

A convenient way for defining common control-surface modes and the associated generalized matrices in standard finite element codes such as MSC/NASTRAN[14] is described in Ref. 15. The method is based on the introduction of huge FMs. The finite element model is modified such that, first, each control surface is disconnected from its actuator. The differential motion between the two sides of each disconnection point defines a new degree of freedom δ_i that represents the rigid-body rotation of the control surface relative to the wing. Each δ_i is loaded with an FM matrix $[M_{H_i}]$ of a very large magnitude (orders of magnitude larger than the entire aircraft). The resulting modes include the control modes $[\phi_{ac}]$ as rigid-body modes (in addition to those of the aircraft), whereas the other modes and their associated natural frequencies and generalized masses are practically equal to those of the original structure.

The technique for generating control modes is expanded here to be applicable to any deformation command to structural elements, including piezoelectric patches. These are actually static deformation shapes caused by a static unit command, 1 V in our case.

The new procedure for the definition of control modes $[\phi_{ap}]$ starts in the finite element modeling. The actuator–structure interface grid points are duplicated with one set remaining connected to the structure and the other set connected to the actuators (piezoelectric elements in our case) only. A scalar point whose displacements represent the piezoelectric command v_{p_i} is defined for each actuator. The actuator-side displacements are then connected to the structure-side ones by the multipoint constraint (MPC) equation

$$\begin{Bmatrix} u^p_{p_i} \end{Bmatrix} = \begin{Bmatrix} u_{p_i} \end{Bmatrix} - \begin{Bmatrix} x_{c_i} \end{Bmatrix} v_{p_i} \tag{16}$$

This is, of course, in contradiction with the fact that the structure-side and the actuator-side displacements are equal. However, the actuator displacements $\{u^p_{p_i}\}$ yield adequate actuator stresses and strains that include the piezoelectric effects.

The control modes can now be calculated in static solutions where unit displacements are enforced at the scalar points representing the control commands. It is more convenient, however, to extract these modes by loading the scalar points by very large masses $[M_H]$ as discussed earlier. The calculated normal modes include n_p control modes of practically zero frequency, whereas the other modes are practically identical to those of the original structure. The FMs $[M_F]$ discussed earlier can still be part of the modeling process and treated as in Eqs. (1–5). With the control modes renormalized for a unit displacement of the relevant scalar point, orthogonality implies that the structural modes are related to the control modes by

$$\begin{bmatrix} \phi_{ah} \\ \phi_{Hh} \end{bmatrix}^T \begin{bmatrix} M_{aa} & 0 \\ 0 & M_H \end{bmatrix} \begin{bmatrix} \phi_{ap} \\ I \end{bmatrix} = [0] \tag{17}$$

where $[\phi_{Hh}]$ contains the participation of the scalar points in the structural modes. The displacements in $[\phi_{Hh}]$ are negligible compared to the other structural displacements in these modes. However, when multiplied by $[M_H]$, they are significant. They can be

used for a convenient calculation of the mass coupling matrix $[M_{hp}]$ between the structural and the control modes, as can be extracted from Eq. (17),

$$[M_{hp}] = [\phi_{ah}]^T [M_{aa}][\phi_{ap}] = -[\phi_{Hh}]^T [M_H] \tag{18}$$

where the right-hand expression is extracted directly from the modal data.

Aeroservoelastic Equations with Piezoelectric Modes

The ASE state-space equations can be constructed with the piezoelectric control modes treated in the same manner as the regular control modes in Eq. (12). The generation of the control modes as part of the normal modes in finite element codes that have an aeroelastic module, that is, MSC/NASTRAN, facilitates the computation of the associated control columns in the tabulated unsteady aerodynamic force coefficient matrices $[Q_{hc}(ik)]$ in a standard run. The rational approximation process to obtain the coefficients of Eq. (11) is performed for these columns in the standard way.[16] The resulting state model is of the form of Eqs. (12) and (13), but with

$$\left\{u_{ae}^p\right\} = \begin{Bmatrix} v_p \\ \dot{v}_p \\ \ddot{v}_p \end{Bmatrix}$$

$$\left[B_{ae}^p\right] = \begin{bmatrix} 0 & 0 & 0 \\ -[\bar{M}]^{-1}[\bar{K}_{hp}] & -[\bar{M}]^{-1}[\bar{B}_{hp}] & -[\bar{M}]^{-1}[\bar{M}_{hp}] \\ 0 & [E_p] & 0 \end{bmatrix}$$

where

$$[\bar{K}_{hp}] = q\left[A_{hp_0}\right], \qquad [\bar{B}_{hp}] = (qb/V)\left[A_{hp_1}\right]$$

$$[\bar{M}_{hp}] = \left[M_{hp} + (qb^2/V^2)A_{hp_2}\right]$$

where the aerodynamic terms associated with the piezoelectric control commands are denoted with subscript p to separate them from the control-surface related terms. The main difference between Eq. (12) with direct piezoelectric forces and that with the control-mode excitation is that the aeroelastic effects due to the piezoelectric command are expressed in the first case as part of the state response, whereas, in the second case, they are part of the control input. As a result, all of the structural parameters in the output equations are now an explicit function of $\{v_p\}$. The element strains, for example, are now expressed in the same manner for the piezoelectric patches and for the rest of the structure by

$$\{\epsilon\} = [EU_a][\phi_{ap} \quad \phi_{ah}] \begin{Bmatrix} v_p \\ \xi \end{Bmatrix} = [\phi_{\epsilon p} \quad \phi_{\epsilon h}] \begin{Bmatrix} v_p \\ \xi \end{Bmatrix} \tag{19}$$

where $[\phi_{\epsilon p}]$ and $[\phi_{\epsilon h}]$ are the modal strain matrices that can be extracted in the normal modes analysis where the control mode and the structural modes are generated simultaneously.

The rest of the ASE modeling process with piezoelectric control modes is similar to that with conventional control surfaces. As in the regular actuator case, piezoelectric commands should also be modeled as driving the patch through a third-order filter (actuator). This is done to allow a proper representation of the mass coupling effects due to $[M_{hp}]$ without having a direct link between the command and the state response. The filters add three states for each piezoelectric patch. This is, of course, a disadvantage compared to the direct actuation modeling described earlier. The roots of this filter should be far enough from those of the aeroelastic plant to avoid nonrealistic interference with the structural response, but not too far to avoid numerical difficulties in the subsequent simulations.

The main advantages of the control-mode approach are that 1) the local vibration modes generated by the FMs in Eq. (1) are not as essential as in the direct force excitation; 2) the explicit appearance of the control columns in the aerodynamic approximation of Eq. (11) may improve their accuracy; and 3) the modal data needed to construct the state-space equations can be extracted from a single standard normal-modes analysis of the structural model, which facilitates a convenient application in common ASE analysis codes such as ZAERO.[17] Some numerical differences between the two modeling approaches are explored in the numerical example.

Numerical Example

The procedures for aeroservoelastic modeling with piezoelectric actuation are demonstrated by the use of the aeroelastic model of an uncrewed aerial vehicle (UAV). The MSC/NASTRAN aircraft structural model of the UAV right-hand side is shown in Fig. 1. The weight of the model is 152 kg. The span of the wing is 4.0 m and the uniform chord length is 0.55 m. The model contains 459 grid points and 580 structural elements. The model is clamped at a fuselage point near the quarter-point of the wing-root chord.

The structural model was modified to include a wing-tip trailing-edge control surface with piezoelectric lead zirconate titanate (PZT) layers patched on the upper and lower skins of the forward one-half of the control surface, as marked in Fig. 1. The patches were modeled as plies of orthotropic material with negligible stiffness in the spanwise direction. The control surface was deflected by a voltage command that expands the upper patch and contracts the lower one in the X directions of the local coordinate systems where the X axes are in the patch planes, pointing to the trailing edge.

The PZT patch properties used for the numerical example are similar to those available with current technology.[2,3] The Young's modulus in the X direction is $E_1 = 6.0E^{10}$ N/m^2, the patch thickness is $t_1 = 0.267$ mm, its chordwise length is $l_c = 52.6$ mm, the free chordwise strain per unit voltage input is $\epsilon_x = 1.74$ μstrain/V, and the maximal voltage input is 1000 V.

It can be observed in Fig. 1 that each patch is connected to six grid points. Because the significant PZT stiffness is only in the X direction, the FM matrix $[M_F]$ introduced in Eq. (1) to generate modes with local deformations is built of six block diagonal matrices

$$\left[M_{F_i}\right] = \begin{bmatrix} m & -m \\ -m & m \end{bmatrix} \tag{20}$$

where $m = 250$ kg. Each $[M_{F_i}]$ is associated with the X directions of one pair of patch-structure interface grid points that have the same Y coordinates. Each $[M_{F_i}]$ is of rank 1, which implies that it adds only one mode of differential motion in X of the two grid points.

Normal modes analysis was performed with symmetric boundary conditions to extract the 26 lowest-frequency modes up to 100 Hz. The frequencies and mode shapes were then corrected by the process of cleaning the FMs of Eqs. (3–5). The natural frequencies with FMs, and those after the cleaning process, are compared in

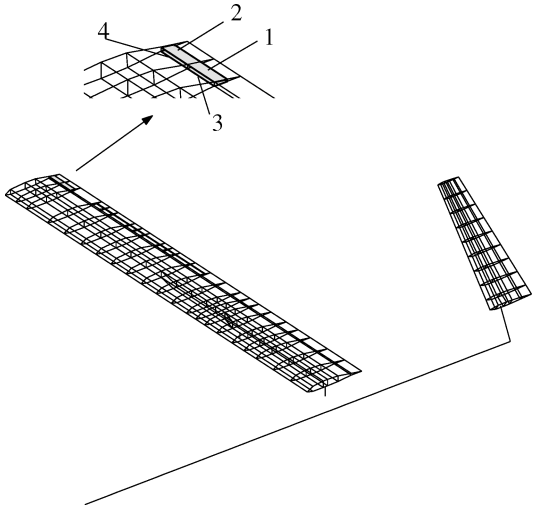

Fig. 1 UAV structural model.

Table 1 Natural frequencies

Mode	Frequency, Hz		
	Original	FM	Cleaned
1	3.6389	3.6389	3.6389
2	6.1324	6.1324	6.1324
3	9.8080	9.8080	9.8080
4	15.4389	15.4389	15.4389
5	16.9169	16.9169	16.9169
6	20.2534	20.2534	20.2534
7	23.0717	23.0716	23.0717
8	36.2334	34.6516[a]	36.2334
9	42.8918	36.2329	42.8918
10	49.5879	36.5234[a]	49.5879
11	50.8109	40.9338[a]	50.8109
12	57.2197	42.8918	57.2197
13	57.8319	43.3431[a]	57.8319
14	59.6411	49.5879	59.6411
15	62.3857	50.8109	62.3858
16	64.1369	57.2187	64.1369
17	83.5643	57.8108	83.5643
18	85.5119	59.6410	85.5119
19	89.0115	61.8811[a]	89.0116
20	99.5916	62.3857	99.5916
21	——	64.1432	565.9400
22	——	66.2260[a]	618.3977
23	——	83.5850	756.4054
24	——	85.5119	4527.1042
25	——	89.0242	5619.3210
26	——	99.5937	5879.6048

[a]Local deformation frequency.

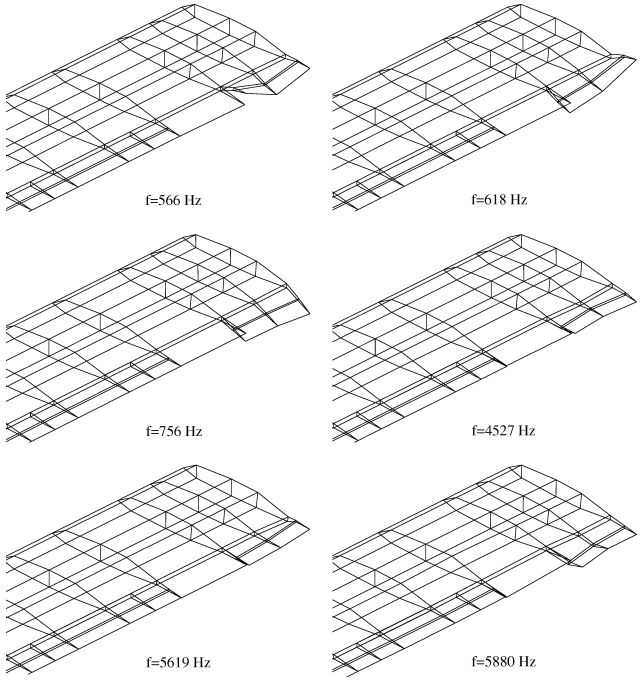

Fig. 2 Normal modes of local PZT-surface deformations.

Table 1 to the original frequencies, calculated from the finite element model without FMs. It can be observed that the FMs added six local-deformation frequencies. Because negligible chordwise deformations near the PZT patches in the original modes, the FMs have a very small effect on the original frequencies. The cleaning process recovers the original frequencies and mode shapes exactly (not shown), and creates six new high-frequency modes that are shown in Fig. 2. It can be observed that the first three modes are of mainly out-of-plane motion, whereas the other three are of in-plane motion.

The control mode of static deformations due to a unit voltage command was generated in two ways, by a static solution with the finite element model, and through normal modes analysis with the dummy mass M_H. The static solution is obtained by the solution of Eq. (7) with the right-hand forces being

$$\{F_a\} = \left[K_{aa}^{p}\right]\left\{x_{c_1}\right\} \tag{21}$$

where $\{x_{c_1}\}$ is a zero vector except for the terms associated with the in-plane X-direction coordinates of the upper patch trailing-edge points, which are $\epsilon_x \times l_c = 9.15E^{-8}$ m each, and those of the lower patch, which are $-9.15E^{-8}$ m each.

The modal solution is performed by duplication of the patch–structure interface points, addition of a scalar point and imposition of the MPC constraints of Eq. (16) with $\{x_{c_1}\}$ of Eq. (21), and loading of the scalar point by the dummy mass $M_H = 10^6$ kg. The resulting frequencies and modes are practically identical to those of the middle column of Table 1, except that the modes include now the control mode with practically zero frequency. This mode is not affected by the FM cleaning process described earlier. However, the participation of the scalar point in the other modes, which forms $\{\phi_{Hh}\}$ of Eq. (18), has to be transformed by Eq. (5) before it is used. Because the calculated control mode is normalized to unit generalized mass, it should be multiplied by 10^3 to obtain the actual control mode. The resulting mode is identical to the one calculated by the direct static solution of Eq. (21).

The static control mode is shown in Fig. 3 with its deflections multiplied by 10^5. With a maximal electric input of 1000 V, the shown shape is 100 times that of the maximal control-surface displacement amplitude with no aerodynamic loads. It reflects a control-surface deflection angle of about 0.6 deg, which means quite small control authority. It may be significant, however, if used with mechanical or aerodynamic amplification measures or with the prospective improvement of smart materials.[2]

The aerodynamic boxes of the doublet-lattice unsteady aerodynamic model are shown in Fig. 4 with the locations of four accelerometers for subsequent ASE analysis. The model consists of seven aerodynamic panels representing four parts of the wing , the aileron, the new control surface (shaded in Fig. 4), and the tail. There were 17 aerodynamic force coefficient matrices $[\bar{Q}_h(ik)]$ at reduced frequency values between $k = 0$ and 3.6 calculated by MSC/NASTRAN for the 27 FM modes, including the control mode,

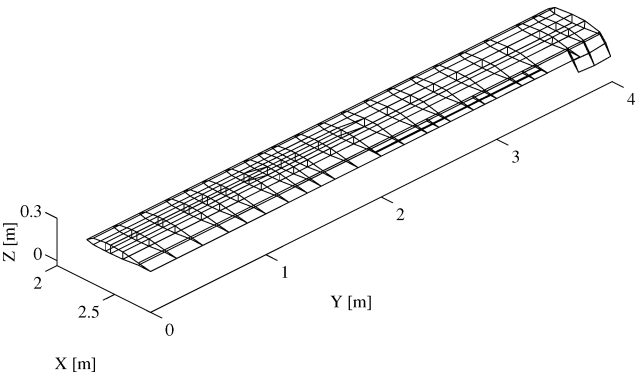

Fig. 3 Static response of the control surface.

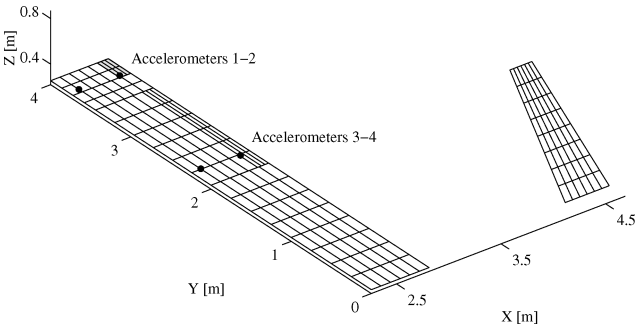

Fig. 4 UAV aerodynamic model.

Table 2 Patch and skin elements strain in microstrains for the input voltage of 1000.0 V

	Static			Steady aerodynamics	
Element	MSC/NASTRAN	Direct-force	Control-mode	Direct-force	Control-mode
Patch-1	−250.4	−251.0	−250.7	−251.6	−251.3
Patch-2	−244.1	−244.7	−244.4	−245.2	−244.9
Patch-3	220.6	221.5	220.5	222.1	221.2
Patch-4	211.0	211.9	211.0	212.5	211.6
Skin-1	530.3	528.1	530.9	528.3	530.8
Skin-2	489.1	488.7	489.7	488.7	489.7
Skin-3	−636.4	−629.6	−636.3	−629.7	−636.2
Skin-4	−596.4	−590.2	−596.3	−590.3	−596.3

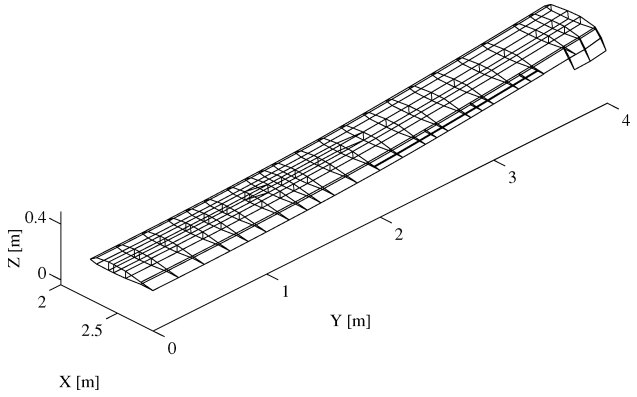

Fig. 5 Static response with aerodynamic forces.

and then transformed to the cleaned modes by

$$[Q_h(ik)] = [\psi]^T [\bar{Q}_h(ik)][\psi] \tag{22}$$

The aerodynamic matrices served as tabulated data for the rational aerodynamic approximation of Eq. (11), with the control terms based on the control-mode aerodynamics. The approximation was performed by the ZAERO code[17] with six aerodynamic lag terms, physical weighting of the tabulated data, and with the steady aerodynamics constrained to match the data at $k = 0$. The approximation coefficients were then used by ZAERO to construct the state-space equations with direct piezoelectric control forces, Eq. (12), and those with the control input replaced by the control-mode formulation. The two models have 52 structural states and 6 aerodynamic states. The output equations were set up to provide the displacement and acceleration at accelerometer 1, the chordwise strains in the four PZT elements, and those in one of the composite layers of the skin elements to which the PZT elements are patched. The state-space matrices were exported to MATLAB® for the remaining analyses in this work.

The demonstration of the two modeling approaches started with the calculation of the steady-state response to a static piezoelectric command of 1000 V at airspeed $V = 50$ m/s. The deformed wing shape with the deformations multiplied by 100 is shown in Fig. 5. The two approaches gave practically identical results. However, the modal responses in the two cases are significantly different. Whereas the control-induced deformations and the associated aerodynamics result in the direct-force case mainly from the response of the high-frequency local-deformation modes, they are related in the second case, where the response of the high-frequency modes is negligible, mainly due to the control mode.

The static chordwise strains in the four PZT patches marked in Fig. 1, and the strains in the skin elements to which the patches are connected are compared in Table 2 to those obtained with no aerodynamics. The modal direct-force strains were calculated with the output Eqs. (14) and (15), whereas the modal control-mode strains were calculated by Eq. (19). The strains in the no-aerodynamics case, as calculated by a full MSC/NASTRAN solution, are also shown in Table 2. Note that the PZT patches and the skin elements have strains of opposite signs, as expected, and that the aerodynamic forces have

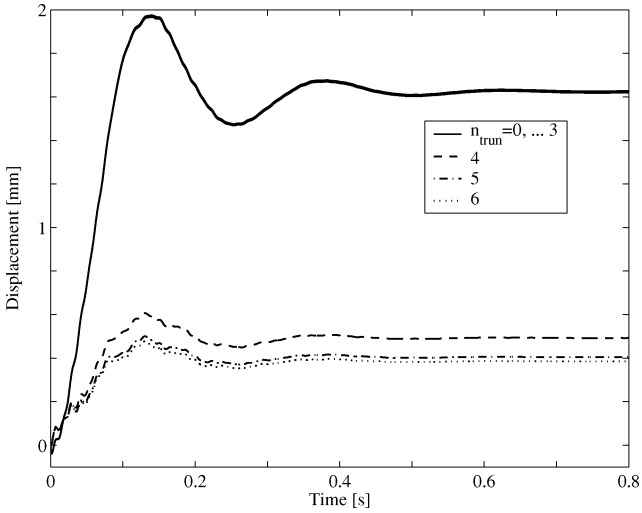

Fig. 6 Displacement response at accelerator 1 to maximal PZT step excitation, direct-force approach.

very small effects on the actuator strains in this case. The control-mode results are somewhat closer to those of MSC/NASTRAN. This is because the direct-force response is more sensitive to numerical errors in accumulating the various modal contributions, as is also shown later.

The aeroelastic models were use in step-response and frequency-response analyses at $V = 50$ m/s with MATLAB. The step response at accelerometer 1 to an input command of 1000 V is shown in Fig. 6 for seven mode truncation cases. The first case is with all of the 26 elastic modes taken into account. The other six cases are with one–six high-frequency modes truncated, starting with the highest one. The first four cases are practically identical because of the in-plane deformation nature of the highest modes. The truncation of four modes and more cause unacceptable errors. It is obvious that the FMs used in the modal data generation were essential. The same seven cases are repeated with the control-mode approach in Fig. 7. All of the cases now give identical results, which implies that the use of FMs had no effect in this case. The slight differences between the direct-force and the control-mode responses with no truncation are related to the higher error level in the direct-force case. The same modal truncation cases are repeated in Figs. 8 and 9, for the acceleration frequency response (in meters per square second) to sinusoidal excitation with an amplitude of 1000 V. The differences are similar in nature to those of Figs. 6 and 7. Note that the truncation errors at the peaks in the high-frequency range of Fig. 8 are smaller than at the low frequencies.

Step response cases are shown in Fig. 10 for the chordwise strain in the PZT patch element 1 (Fig. 1). The strain at $t = 0$ is that of the constrained patch before the motion starts. It converges rapidly to the actual steady strain of Table 2 when the skin deforms. Large errors are observed when modes are truncated, even with the truncation of the three highest-frequency modes only. Similar behavior is shown in Fig. 11 for the skin element to which the patch element is attached.

The strain step responses are repeated in Figs. 12 and 13 with the control-mode approach. Even though they converge to almost the

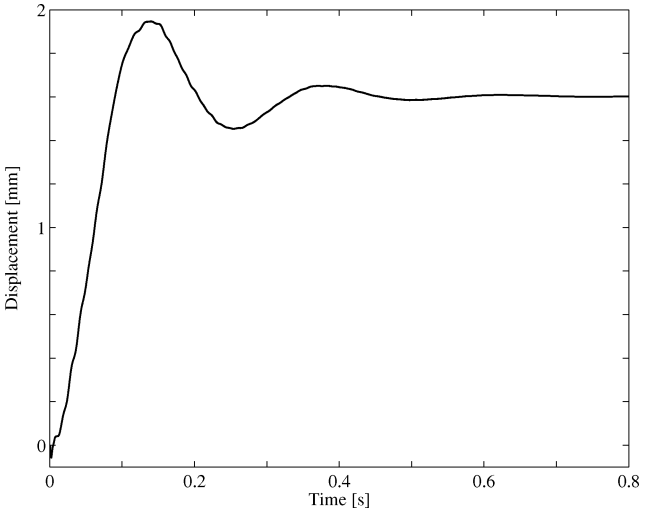

Fig. 7 Displacement response at accelerator 1 to maximal PZT step excitation, control-mode approach.

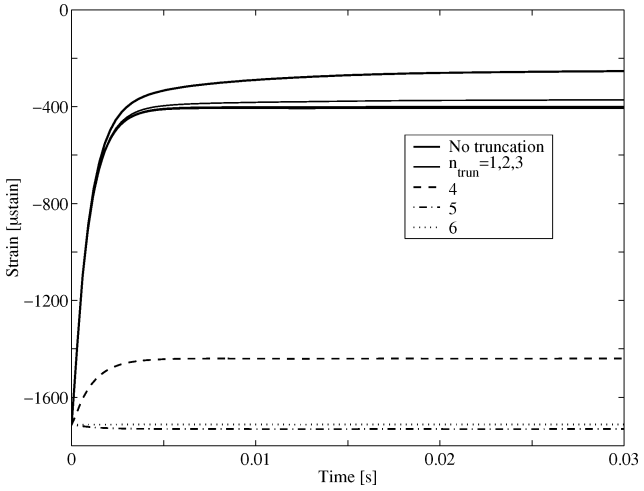

Fig. 10 Strain response at patch element 1 to maximal PZT step excitation, direct-force approach.

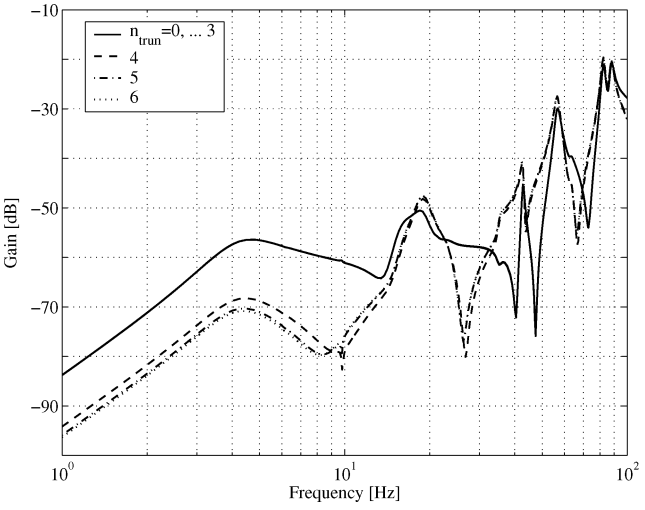

Fig. 8 Acceleration response at accelerator 1 to maximal PZT sinusoidal excitation, direct-force approach.

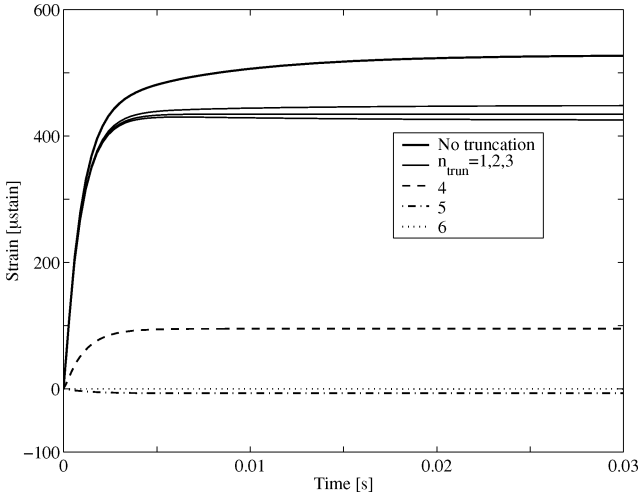

Fig. 11 Strain response at skin element 1 to maximal PZT step excitation, direct-force approach.

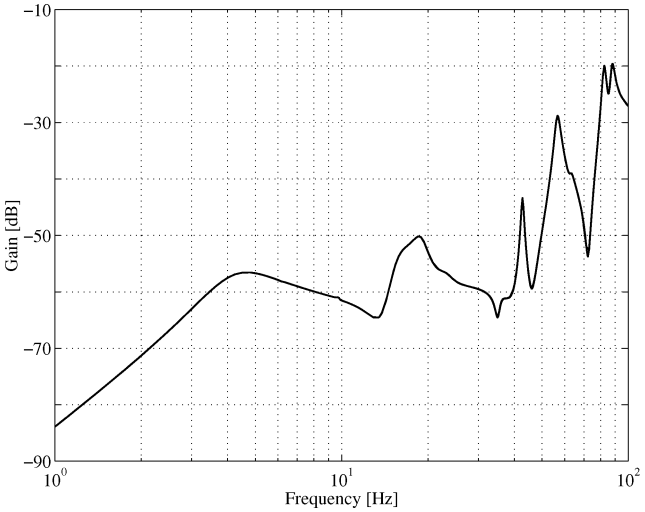

Fig. 9 Acceleration response at accelerator 1 to maximal PZT sinusoidal excitation, control-mode approach.

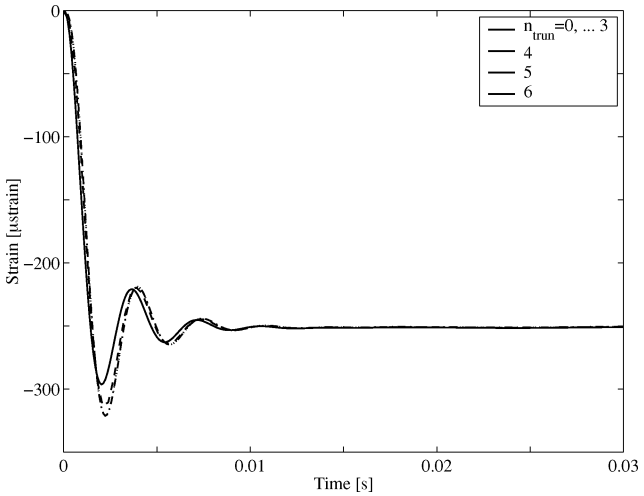

Fig. 12 Strain response at patch element 1 to maximal PZT step excitation, control-mode approach.

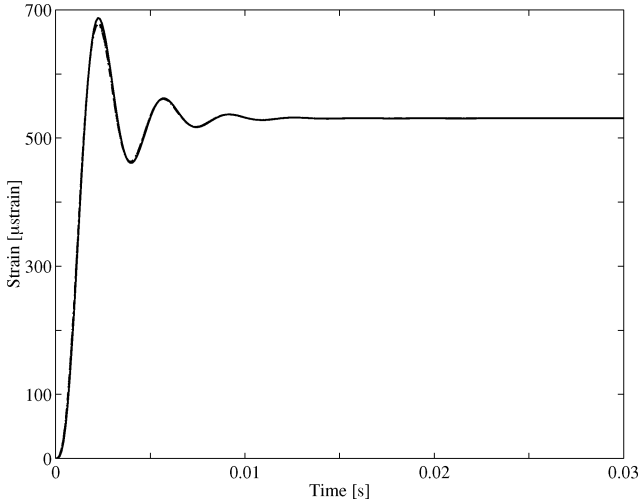

Fig. 13 Strain response at skin element 1 to maximal PZT step excitation, control-mode approach.

same strain values as in the direct-force case, the time histories are substantially different than those of Figs. 10 and 11. The reason is that the actuation dynamics are different in the two cases. Whereas the forces in the direct-force case introduce significant structural loads from $t = 0$, they pass in the control-mode case through a third-order filter that was added to the model as discussed after Eq. (19). The added filter may have an important role in alleviating the high patch strains observed in Fig. 10. Another important aspect of Figs. 10 and 13 is that the truncation of four–six modes introduces about a 10% error in the peak patch response and about a 2% error in the peak skin response.

Conclusions

Common modal-based state-space equations of motion for aeroservoelastic analysis and design where expanded in this work to accommodate piezoelectric strain actuators. The use of local FM matrices, which are similar to the actuator stiffness matrices, facilitates the essential inclusion of local deformations of the actuators and the surrounding structure in the modal coordinates with a minimal increase of the model order. The state-space equations are developed with the input parameters defined by either the direct-force or the control-mode approach. The direct-force approach does not require the generation of an aerodynamic control mode and the associated approximation coefficients, but its accuracy is shown to be heavily dependent on the presence of local deformations in the modal data, which might cause some numerical difficulties. The control mode can be generated together with the regular vibration modes. The strains in the piezoelectric elements appear in these modes with the piezoelectric control effects included. The local modes due to the use of FMs are not essential when the control-mode approach is used, but may still improve the accuracy of the local strains. The two modeling alternatives are formulated in a way that complies with common finite element and aeroelasticity codes.

References

[1]Crawley, E., "Intelligent Structures for Aerospace: A Technology Overview and Assessment," *AIAA Journal*, Vol. 32, No. 8, 1994, pp. 1689–1899.

[2]Chopra, I., "Status of Application of Smart Structures Technology to Rotorcraft Systems," *Journal of American Helicopter Society*, Vol. 45, No. 4, 2000, pp. 228–252.

[3]Forster, E., and Livne, E., "Integrated Design Optimization of Strain Actuated Structures for Dynamic Shape Control," AIAA Paper 2000-1336, *Proceedings of the 41st AIAA/ASME/ASCE/AHS/ASC Structures, Structural Dynamics, and Materials Conference*, April 2000.

[4]Karpel, M., and Newman, M., "Accelerated Convergence for Vibration Modes Using the Substructure Coupling Method and Fictitious Coupling Masses," *Israel Journal of Technology*, Vol. 13, May 1975, pp. 55–62.

[5]Karpel, M., and Raveh, D., "Fictitious Mass Element in Structural Dynamics," *AIAA Journal*, Vol. 34, No. 3, 1996, pp. 607–613.

[6]Anguita, L., Maderuelo, C., Climent, H., and Karpel, M., "Efficient Flutter Analysis of Aircraft with Multiple External Store Configurations," *Proceedings of the International Forum on Aeroelasticity and Structural Dynamics*, Vol. II, Editorial Alfasur, Madrid, Spain, 2001, pp. 333–346.

[7]Livne, E., "Accurate Calculation of Control Augmented Structural Eigenvalue Sensitivities Using Reduced-Order Models," *AIAA Journal*, Vol. 27, No. 7, 1989, pp. 947–954.

[8]Karpel, M., and Wieseman, C. D., "Modal Coordinates for Aeroelastic Analysis with Large Local Structural Variations," *Journal of Aircraft*, Vol. 31, No. 2, 1994, pp. 396–403.

[9]Karpel, M., and Wieseman, C. D., "Time Simulation of Flutter with Large Stiffness Changes," *Journal of Aircraft*, Vol. 31, No. 2, 1994, pp. 404–410.

[10]Karpel, M., and Presente, E., "Structural Dynamic Loads in Response to Impulsive Excitation," *Journal of Aircraft*, Vol. 32, No. 4, 1995, pp. 853–861.

[11]Karpel, M., Raveh, D., and Ricci, S., "Ground Vibration Tests of Space-Structure Components Using Boundary Masses," *Journal of Spacecraft and Rockets*, Vol. 33, No. 2, 1996, pp. 272–277.

[12]Karpel, M., and Ricci, S., "Experimental Modal Analysis of Large Structures by Substructuring," *Mechanical Systems and Signal Processing*, Vol. 11, No. 2, 1997, pp. 245–256.

[13]Idan, M., Karpel, M., and Moulin, B., "Aeroservoelastic Interaction Between Aircraft Structural and Control Design Schemes," *Journal of Guidance, Control, and Dynamics*, Vol. 22, No. 4, 1999, pp. 513–519.

[14]Blakely, K., *MSC/NASTRAN Basic Dynamic Analysis*, ver. 68, MacNeal–Schwendler Corp., Los Angeles, CA, 1993.

[15]Karpel, M., "Multidisciplinary Optimization of Aeroservoelastic Systems Using Reduced-Size Models," *Journal of Aircraft*, Vol. 29, No. 5, 1992, pp. 939–946.

[16]Karpel, M., "Time Domain Aeroservoelastic Modeling Using Weighted Unsteady Aerodynamic Forces," *Journal of Guidance, Control, and Dynamics*, Vol. 13, No. 1, 1990, pp. 30–37.

[17]"ZAERO Version 7.0 Theoretical Manual," ZONA 02-12.4, ZONA Technology, Scottsdale, AZ, Nov. 2003.